

Article

Identification of Zn-Bearing Micas and Clays from the Cristal and Mina Grande Zinc Deposits (Bongará Province, Amazonas Region, Northern Peru)

Giuseppe Arfè *, Nicola Mondillo, Giuseppina Balassone , Maria Boni, Piergiulio Cappelletti and Tommaso Di Palma 

Dipartimento di Scienze della Terra, dell'Ambiente e delle Risorse, Università degli Studi di Napoli Federico II, Complesso Universitario di Monte S. Angelo, Via Cintia 26, 80126 Napoli, Italy; nicola.mondillo@unina.it (N.M.); balasson@unina.it (G.B.); boni@unina.it (M.B.); piergiulio.cappelletti@unina.it (P.C.); to.dipalma@virgilio.it (T.D.P.)

* Correspondence: giuseppe.arfe@unina.it

Received: 11 October 2017; Accepted: 3 November 2017; Published: 7 November 2017

Abstract: Zn-bearing phyllosilicates are common minerals in nonsulfide Zn deposits, but they seldom represent the prevailing economic species. However, even though the presence of Zn-bearing clays is considered as a disadvantage in mineral processing, their characteristics can give crucial information on the genesis of the oxidized mineralization. This research has been carried out on the Mina Grande and Cristal Zn-sulfide/nonsulfide deposits, which occur in the Bongará district (Northern Peru). In both of the deposits, Zn-bearing micas and clays occur as an accessory to the ore minerals. The XRD analyses and scanning electron microscopy with energy dispersive X-ray spectroscopy (SEM-EDS) investigations revealed that the Zn-bearing micas that are occurring in both deposits mostly consist of I/S mixed layers of detrital origin, which have been partly altered or overprinted by saucnite during the supergene alteration of sulfides. Sporadic hendricksite was also identified in the Cristal nonsulfide mineral assemblage, whereas at Mina Grande, the fraipontite-zaccagnaite (3R-polytype) association was detected. The identified zaccagnaite polytype suggests that both fraipontite and zaccagnaite are genetically related to weathering processes. The hendricksite detected at Cristal is a product of hydrothermal alteration, which is formed during the emplacement of sulfides. The complex nature of the identified phyllosilicates may be considered as evidence of the multiple processes (hydrothermal and supergene) that occurred in the Bongará district.

Keywords: Zn-micas; Zn-clay minerals; Bongará; northern Peru; XRPD; SEM-EDS

1. Introduction

The Zn-nonsulfide deposits have been genetically associated to both hypogene (hydrothermal) and supergene (weathering) processes [1–3]. The geology, the nature of the protore and climate are the main controls on the genesis and mineral association of supergene deposits. The most common mineral phases in the Zn-nonsulfide deposits are smithsonite, hydrozincite, hemimorphite, and saucnite, with local cerussite and anglesite occurrences [1]. Minor components can be represented by phosphates, vanadates, and Fe-oxy-hydroxides. Zinc-rich clay minerals are seldom the prevailing economic species in nonsulfide ores, with the exception of the peculiar case of the Skorpion deposit in Namibia [4,5]. In fact, their presence is commonly considered as a disadvantage in the first steps of mineral processing [6,7]. The particle size and fabric of minerals belonging to smectite and vermiculite groups can be a problem during gravity separation and flotation processing [8–10]. This generally results in a slower flotation kinetics [11,12] and detrimental effects on the leaching techniques, due to “undesired” increments of pulp viscosity. Therefore, to understand the nature of clays occurring in

the paragenesis of nonsulfide ores is a crucial issue when planning the correct workflow and mineral processing procedure, in order to avoid any loss during base and critical metal extraction and recovery. Huge steps forward in the field of nonsulfide exploitation and recovery have been done since the discovery of the Skorpion deposit, where the main nonsulfide mineral is represented by sauconite (Zn-smectite). To overcome the mentioned processing issues, and to maximize the zinc recovery, the solvent extraction technique was applied at Skorpion [13], coupled with several electrowinning and leaching steps [14,15].

Even though the nature of clays is crucial information for the mining industry dealing with nonsulfide deposits, the knowledge of the genesis of such minerals is also an interesting issue from the scientific point of view. Zn-smectite (e.g., sauconite) is commonly related to the hydrolysis of aluminosilicate minerals, such as micas and feldspars [4,5] under meteoric conditions ($T = 20\text{--}25\text{ }^{\circ}\text{C}$) and atmospheric pressure [16,17], and at neutral pH or nearly below 7 in prevailing arid climate settings [18,19]. However, experimental studies on the synthesis and stability of sauconite [20–24] revealed that it can also form at $T = 200\text{ }^{\circ}\text{C}$ and pH of up to 12. Kaolinite, usually formed under tropical climates, acidic conditions, and high water/rock ratios [19,25], is rare in nonsulfide deposits. Less uncommon, instead, is fraipontite, which is a mineral belonging to the kaolinite-serpentine group [26,27]. Fraipontite can be hydrothermal in origin, as in the case of the Preguiça mine in southern Portugal [28], or associated with late stages of the supergene evolution [26,27]. Since neither the kaolinite-serpentine minerals, nor the clays belonging to the smectite group are really useful in discriminating between supergene or hydrothermal origin, in several studies [27,29–31] where a clear identification of the Zn-bearing clay minerals has been provided, several doubts still remain on their formation. On the contrary, the Zn- and Mn-bearing micas may be a precious source of genetic information for nonsulfide Zn deposits, because they commonly form through hydrothermal processes at high temperatures ($>150\text{ }^{\circ}\text{C}$). In fact, the synthesis of Mn-bearing micas has been achieved only under hydrothermal conditions at a temperature of around $200\text{ }^{\circ}\text{C}$ [32]. In magmatic and metamorphic environments, zincian trioctahedral micas (Zn-Mn-bearing fluorophlogopite, hendricksite) are seldom observed and, when present, indicate skarn conditions and/or low $f\text{S}_2$, high $f\text{O}_2$, high alkalinity and high volatiles content in their parental magma [33], and references therein.

The main aim of this study is to identify the Zn-bearing phyllosilicates that are occurring in the Mina Grande and Cristal sulfide and nonsulfide deposits, located in the Bongará area, belonging to the Subandean fold and thrust belt of northern Peru (Figure 1). Sulfide minerals are mostly represented by sphalerite and less pyrite that have been weathered to a nonsulfide assemblage, consisting of goethite, smithsonite, hemimorphite, and hydrozincite. Minor amounts of various Zn-bearing phyllosilicates were also identified in these deposits [34,35], but no specific analyses on clay minerals have been carried out yet.

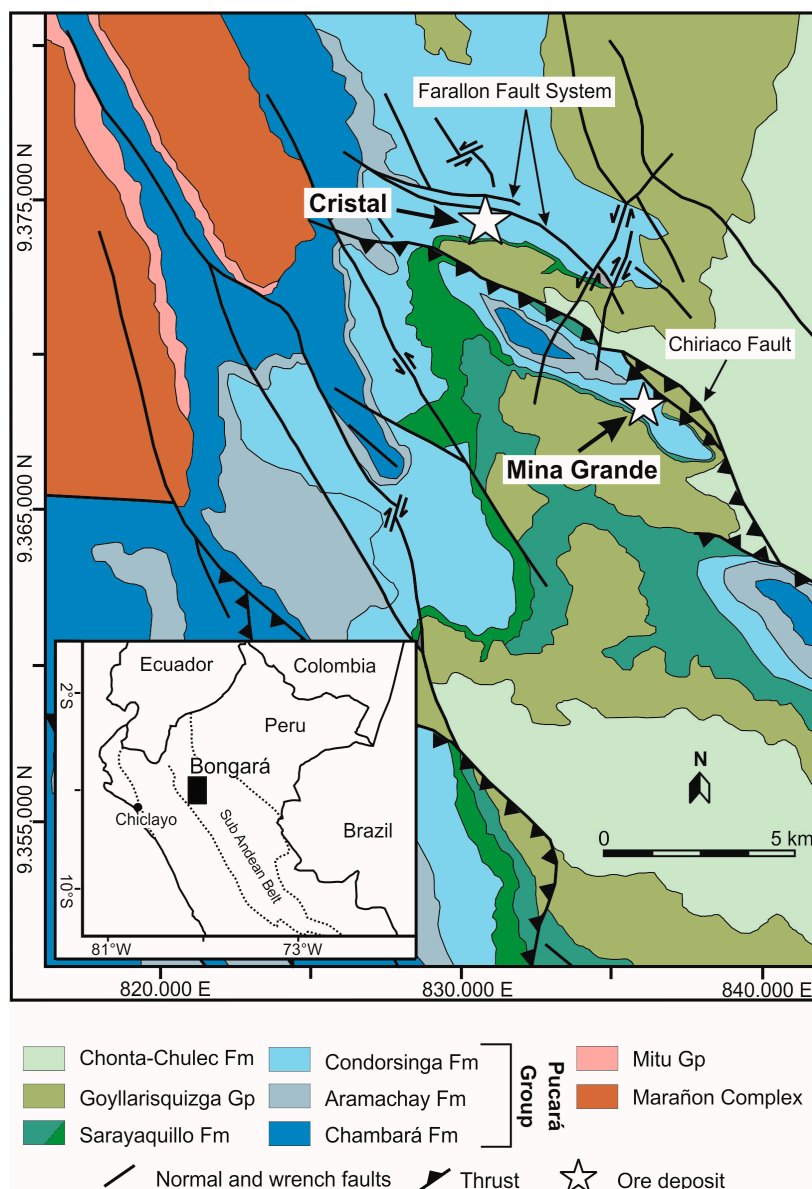


Figure 1. Location of the Bongará province within the Sub Andean Belt and geological map of the Mina Grande and Cristal areas modified from [34].

2. Geological Setting

The Cristal and Mina Grande mineralizations are hosted by the sedimentary successions of the Pucará Group (Figure 1), which lie on top of the continental sequences of the Middle—Late Triassic Mitu Group [36,37], in turn overlying the Paleozoic metamorphic basement (i.e., the Marañon Complex; Reid, 2001; Mišković et al., 2009) [38,39]. The Pucará Group is subdivided in three prevalingly carbonate formations that from the stratigraphic base to the top are as follows (Figure 1): (1) Upper Triassic Chambará Formation; (2) Upper Triassic—Lower Jurassic Aramachay Formation; and, (3) Lower Jurassic Condorsinga Formation [36,40–42]. The Chambará and Condorsinga Formations are dominated by shallow-water platform facies in contrast with the Aramachay Formation, which is deeper basinal. The Pucará successions are followed by continental sequences of the Sarayaquillo Formation (Upper Jurassic—Cretaceous) [36,43], and by the marine lithologies of the Lower Cretaceous Goyllarisquizga Group and the Chonta-Chulec Formation [44]. The study area was affected by Neogene

tectonics, characterized by late Miocene and Pliocene—early Pleistocene uplift phases, corresponding to the Andean and Quechua tectonic pulses [45–47].

2.1. Cristal Prospect

The Cristal prospect is located in a faulted block, which is bordered by the Chiriaco reverse fault and the South Farallon normal fault (Figure 1). The zinc occurrences consist of both sulfide and nonsulfide bodies [35,48,49], discontinuously cropping out over an area of ca. 2 km². The mineralized bodies are mainly hosted by dolomitized limestone of the upper levels of the Condorsinga Formation, alternated with clayey horizons [48,50–52]. Limestone is extensively karstified, with reworked carbonate material in the form of layered infills to fossil solution cavities and cave systems. The clayey layers consist of quartz, feldspar, mica, and clays, which are associated with detrital monazite, xenotime and zircon. The bulk mineralogy of the drillcore samples [35] is characterized by ubiquitous quartz and muscovite. The mineralogy of the sulfide bodies is relatively simple, and mostly consists of disseminated dark-brown and Fe-rich sphalerite [49,53], with lesser amounts of pyrite and galena. The nonsulfide mineral association is quite complex, being represented by a wide suite of supergene minerals: smithsonite, hemimorphite, hydrozincite, chalcophanite, goethite, and greenockite [35]. Smithsonite prevails over hemimorphite, with abundances that are between 10 and 70 wt %, whereas hemimorphite ranges from 5 to 60 wt %. Goethite has concentrations that vary between ~2 and ~35 wt %. In addition, in the Cristal drillcores, sauconite (<5 wt %), as well as minor amounts of a Zn-Mn-bearing mica, tentatively identified as hendricksite, were also detected [35].

2.2. Mina Grande Deposit

The Mina Grande deposit is located ~6 km south of Cristal, on top of an anticlinal ramp in the hangingwall of the Chiriaco reverse fault (Figure 1) [34,54]. Compared to the Cristal deposit, the zinc occurrences at Mina Grande consist almost exclusively of Zn-oxidized minerals, whereas sulfides are very rare. The host rock of the nonsulfide mineralization is predominantly a limestone belonging to the upper levels of the Condorsinga Formation, with intercalations of siliciclastic material: quartz and feldspar, with minor monazite, xenotime, and zircon [34]. The nonsulfide mineralization occurs as accumulations in karst depressions and cavities, commonly in form of collapse breccias. The karst cavities developed during the Miocene—Pliocene Andean tectonics, along northwest-southeast fractures and faults and locally along stratification joints, and overprinted the Cretaceous karstified surface of the Condorsinga Formation. Nonsulfide association consists of hydrozincite, hemimorphite, smithsonite, and Fe-(hydr)oxides [34]. In the samples analyzed for this study, hydrozincite (from 25 to 45 wt %) prevails over hemimorphite and smithsonite (between 5 and 40 wt %). At Mina Grande the Zn-phyllosilicate fraipontite was tentatively identified, commonly occurring as alteration rims around muscovite and other types of undetermined Zn-bearing micas [34].

3. Materials and Methods

The analyses were conducted on 12 clay-rich samples from several drillcores of the Cristal prospect (CR02, CR03-3, CR03-4, CR07-9, CR07-11, CR07-13, CR07-14, CR13-5, CR13-6, and CR13-7), and on mineralized outcrop samples (ZB-1 and ZB-2) from the Mina Grande deposit (Figure 2).

The samples were cut in small slabs for the preparation of polished thin sections used for optical microscopy (OM) and scanning electron microscopy with energy dispersive X-ray spectroscopy (SEM-EDS). SEM and backscattered electron (BSE) observations on thin sections were performed on a JEOL JSM5310 (DiSTAR-Department of Earth Sciences, Environment and Resources, Napoli, Italy). The analytical conditions were: 20 mm objective lens to specimen working distance, 15 kV accelerating voltage with a tilt angle of 0°. Analytical errors are 1% relative for major elements and 3% relative for minor elements. Element mapping and qualitative energy dispersive (EDS) investigations were carried out with the INCA X-stream pulse processor and the 4.08 version Inca software (DiSTAR, Napoli, Italy), interfaced with the JEOL JSM 5310.

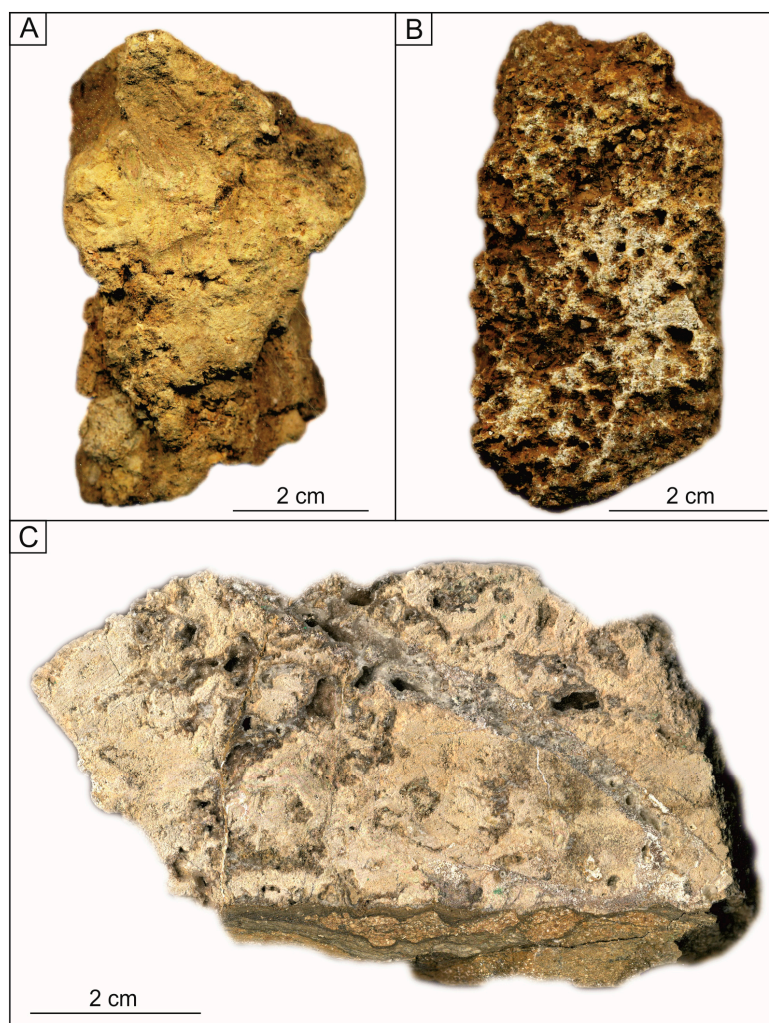


Figure 2. Examples of analyzed specimens from Cristal (A) CR07-14; (B) CR13-7 and Mina Grande (C) ZB-2 deposits.

X-ray powder diffraction (XRPD) analyses on oriented clay aggregates were conducted on the clay fraction of seven samples (CR02, CR07-11, CR07-13, CR07-14, CR13-7, ZB1, and ZB2). To obtain the clay fraction, according to the Moore and Reynolds [55] procedure, the samples were milled and ground, and about 30 g of grained material (grain size < 1 mm) was blended with 500 mL of deionized water in a plastic beaker to be subjected to ultrasonic disaggregation for about 15 min. The <2 μm fraction was separated from the whole sample via four steps of progressive sedimentation (1 min, 5 min, 1 h, and 17 h “overnight”), and two cycles of centrifugation with a Hettich Rotina centrifuge (5 min at 5000 rpm and 40 min at 8000 rpm). The final suspension that resulted was too dilute, and thus, for the preparation of oriented aggregates (mounts), we used the suspended material that was obtained after the first or the second cycle of centrifugation, depending on the quantity of material. This material was smeared on glass slides and left drying at an ambient temperature (air-dried). The slides were firstly solvated with Ethylene-glycol (EG) at 80 °C for 24 h [56], and then heated at 350 °C for 2 h. Subsequently, the presence of kaolinite was investigated by heating the slides at 550 °C for 1 h [55]. XRPD analysis was performed on (i) the overnight residues of randomly oriented mounts (labelled “O/N”); (ii) air-dried oriented mounts (labelled “AON”); (iii) glycolated (EG) oriented samples (labelled “AOG”); and, (iv) oriented samples heated at 350 and 550 °C, respectively labelled as “AOR” or “AORR”. The XRPD analyses were carried out on a Seifert GE ID3003 diffractometer (DiSTAR, Napoli, Italy), with Cu K α radiation, Ni-filtered at 40 kV and 30 mA, 3–70° 2 θ range, step

scan 0.02° , time 10 s/step, and the RayfleX (GE) software package; a silicon wafer was used to check the instrumental settings.

In order to obtain morphologic SEM images of clayey material, representative chips (ca. 5 mm \times 5 mm in dimension) were directly removed from the AON oriented aggregate slides, and were mounted on Agar stubs using Carbon conductive double-sided adhesive tape.

4. Results

4.1. XRPD Analysis on Oriented and Randomly Oriented Mounts

Random XRPD patterns of the O/N overnight residues (Figure 3A,B) show that, after the first three steps of progressive sedimentation, the samples still contain quartz, calcite, goethite, smithsonite, hydrozincite, and hemimorphite, in addition to the layered silicates. The XRD patterns of the AON (air-dried) slides show that 10 Å-spaced phyllosilicates mainly occur in the samples CR02, CR07-11, CR07-13, CR07-14 and CR13-7, whereas 15 Å-spaced phyllosilicates are dominant in the samples CR07-14, and CR13-7 (Figure 4).

The AOG EG-treated patterns of the CR07-14 and CR13-7 samples (Figure 4A,B, respectively) show a shift in the reflection at 15 Å toward 17.8 Å, due to the swelling typical of the smectite clays. In the AOG EG-treated pattern of the sample CR07-14, a decoupling of the ~ 10 Å peak into the 10.3 and 9.97 Å reflections was also observed (Figure 4A). After a treatment at 350 °C, the decoupling disappeared and a single reflection appeared at ~ 10 Å, which was sharper than the previous one that was observed in the AON (air-dried) pattern (Figure 4A). This behavior suggests that the original reflection at 10 Å could correspond to a mixed layer illite-smectite (I/S), and that the narrow shoulder appearing at 10.3 Å in the EG-treated pattern likely represented the (001) illite reflection. The ~ 10 Å position of the I/S mixed layer reflection indicates a long-range ordering (*Reichweite value* "R" > 1) and a high percentage of illite (>90%) in the mixed-layer I/S [55]. Sample CR13-7 does not show this decoupling (Figure 4B).

The AON, AOG, and AOR patterns of samples CR07-14 and CR02 (Figure 4A,C, respectively) show the presence of a peak at around 7.1 Å, which is very weak or absent in other samples (e.g., samples CR13-7). The disappearance of the 7.1 Å-peak in the AORR pattern (550 °C-heated slides) of both CR07-14 and CR02 samples suggests that the reflection can be likely attributable to the presence of kaolinite, rather than chlorite [55].

In the air-dried samples from the Mina Grande deposit (e.g., sample ZB-1; Figure 4D), the main reflections are related to hydrozincite (i.e., 6.66 Å). Minor reflections occur at 3.03, 7.07, 7.53, and 10 Å. The 7.07 Å reflection represents the basal spacing 001 of fraipontite, whereas the 7.53 Å reflection corresponds to the 003 spacing of zaccagnaite $[\text{Zn}_4\text{Al}_2(\text{CO}_3)(\text{OH})_{12}\cdot 3\text{H}_2\text{O}]$, a mineral belonging to the hydrotalcite-manasseite group [57–59].

The occurrence of fraipontite and zaccagnaite is confirmed by the distinct presence of other diagnostic reflections for both fraipontite (d_{002} at 3.53 Å and d_{201} at 2.48 Å) and zaccagnaite (d_{006} at 3.76 Å, d_{012} at 2.58 Å) (Figure 3B). The XRPD pattern of zaccagnaite occurring in the O/N overnight residue of sample ZB-1 (Figure 3B) belongs to the zaccagnaite-3R polytype [59].

In the Mina Grande samples (ZB-1 and ZB-2), the 060 spacings occurring in the O/N (overnight residues) patterns (Figure 3B) between 1.53 and 1.54 Å are consistent with the presence of trioctahedral species of the serpentine (fraipontite) group. In both Mina Grande and Cristal samples (ZB-1 and CR07-14, respectively), broader 060 reflections between 1.49 and 1.50 Å may correspond to species of the smectite group or to illite/smectite mixed layers (Figure 3B). The 2.98 Å ($30^\circ 2\theta$) reflections, which are visible in both Cristal (CR02) and Mina Grande (ZB-2) samples (Figure 3A), suggest the presence of the $2M_1$ mica polytype [55].

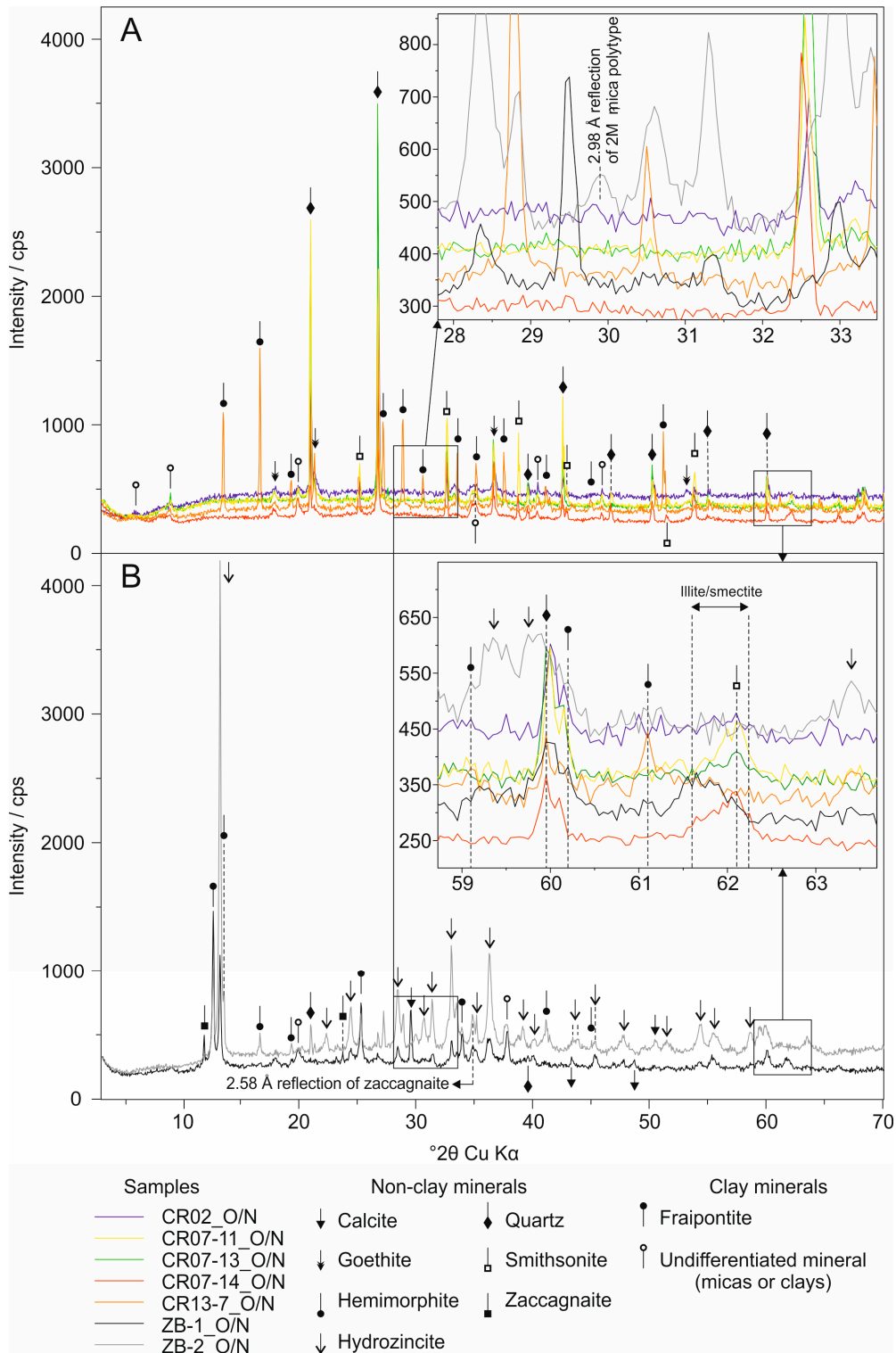


Figure 3. X-ray powder diffraction (XRPD) patterns of randomly oriented (O/N) residues of Cristal (A) and Mina Grande (B) samples, which show the main reflections of the detected minerals, those corresponding to the 060 spacings and the diagnostic 2.98 Å peak of the 2M₁ mica polytype.

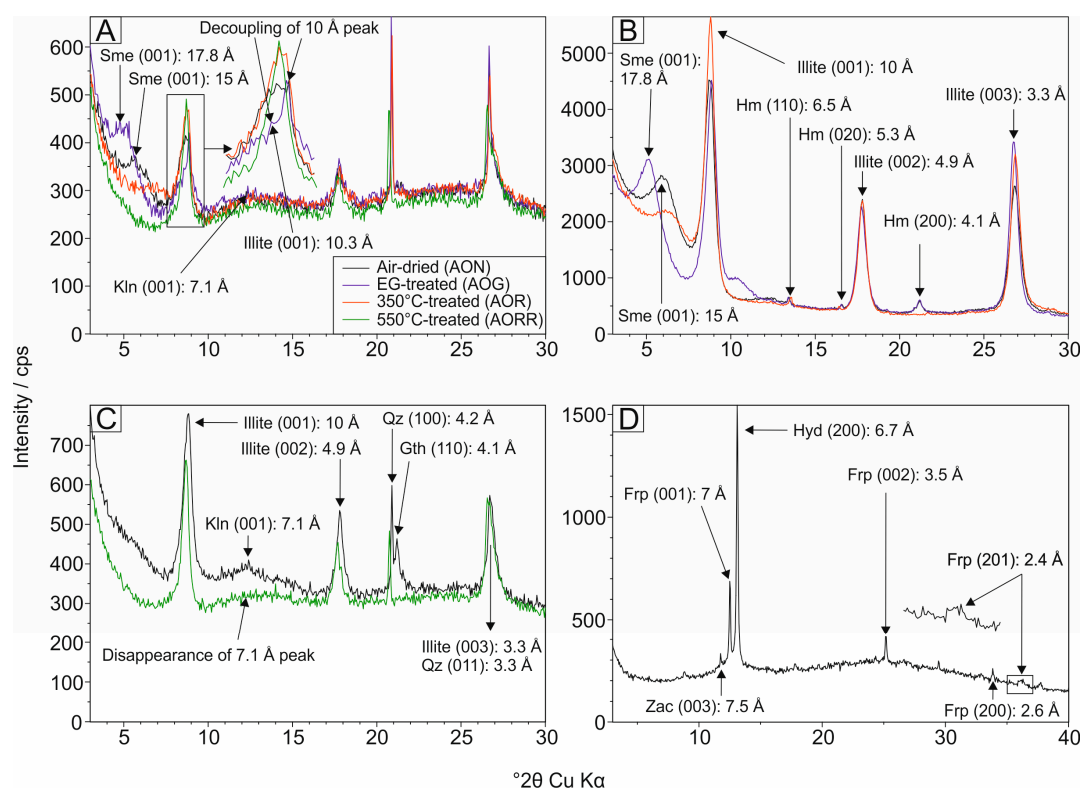


Figure 4. XRPD patterns of AON, AOG, AOR, and AORR oriented aggregates from residues of 5 min/5000 rpm and 40 min/8000 rpm centrifugation cycles. (A) The XRPD patterns of the Ethylene-glycol (EG)-treated aggregate (AOG) show the decoupling of the 10 Å peak (AON) into 10.3 (left) and 9.97 (right) Å reflections (sample CR07-14_5/5000); (B) Example of I/S mixed layers in the Cristal samples. Hemimorphite (Hm) residues are still detectable in the sample (CR13-7_40/8000); (C) The XRPD patterns of the AOR oriented aggregate show the disappearance of the 7.1 Å reflection of kaolinite (Kln) (sample CR02_5/5000); (D) The XRPD pattern of the AON oriented aggregate shows the diagnostic reflections of fraipontite (Frp) and the 003 spacing of zaccagnaite (Zac) in a hydrozincite-rich sample from the Mina Grande deposit (sample ZB-1_5/5000).

4.2. Chemical Composition and SEM Observations

In the analyzed samples, the most common micas, occurring together with detrital apatite, rutile, and quartz in a Zn- and Mn-bearing clayey matrix (Figure 5A), commonly show SiO₂ and Al₂O₃ contents (Table 1), respectively, which are higher and lower than the values reported for the muscovite classified by International Mineralogical Association (IMA). These micas also have FeOt (total iron) and MgO contents ranging from 0 to 5 wt %, and from 0 to 3 wt %, respectively, and concentrations of interlayer cations varying from 6 to 11 wt % for K₂O and <1 wt % for CaO. Several Bongará micas are also Zn-bearing (up to 12 wt % ZnO; Table 1). These compositions are not compatible with proper muscovite, and could evidence the presence of illite or I/S mixed layers.

In the mica-rich samples, it was possible to detect Zn-Mn-bearing phyllosilicates with compositions that are close to hendricksite [K(Zn,Mg,Mn)₃Si₃AlO₁₀(OH)₂], which locally replace Zn-bearing illite or I/S mixed layers (Figure 5B), and also occur as thin interstratifications within the mica flakes (Figure 5C,D). However, the ZnO, SiO₂, and Al₂O₃ contents (Table 2) detected in the Zn-Mn-bearing phyllosilicates do not coincide exactly with theoretical hendricksite (IMA database). Generally, the SiO₂ and Al₂O₃ contents of Bongará hendricksite-like phases are higher and the ZnO contents are lower than the in IMA hendricksite, as well as its SiO₂/Al₂O₃ ratio (2.30 for IMA hendricksite and 1.73 for Cristal Zn-Mn-bearing micas). The common association of Zn-Mn-bearing phyllosilicates with Mn-(hydr)oxides, sometimes finely intergrown with layered minerals, makes

it difficult to discriminate by SEM-EDS the Mn content that is related to each phase (Figure 5C,D). However, qualitative SEM-EDS analyses, performed on small portions of the clay fraction apparently free of Mn-(hydr)oxides (Figure 5E,F), led to confirm that the phyllosilicates in the clay fraction were free of Mn-(hydr)oxides, thus corroborating the occurrence of Zn-Mn-bearing phyllosilicates.

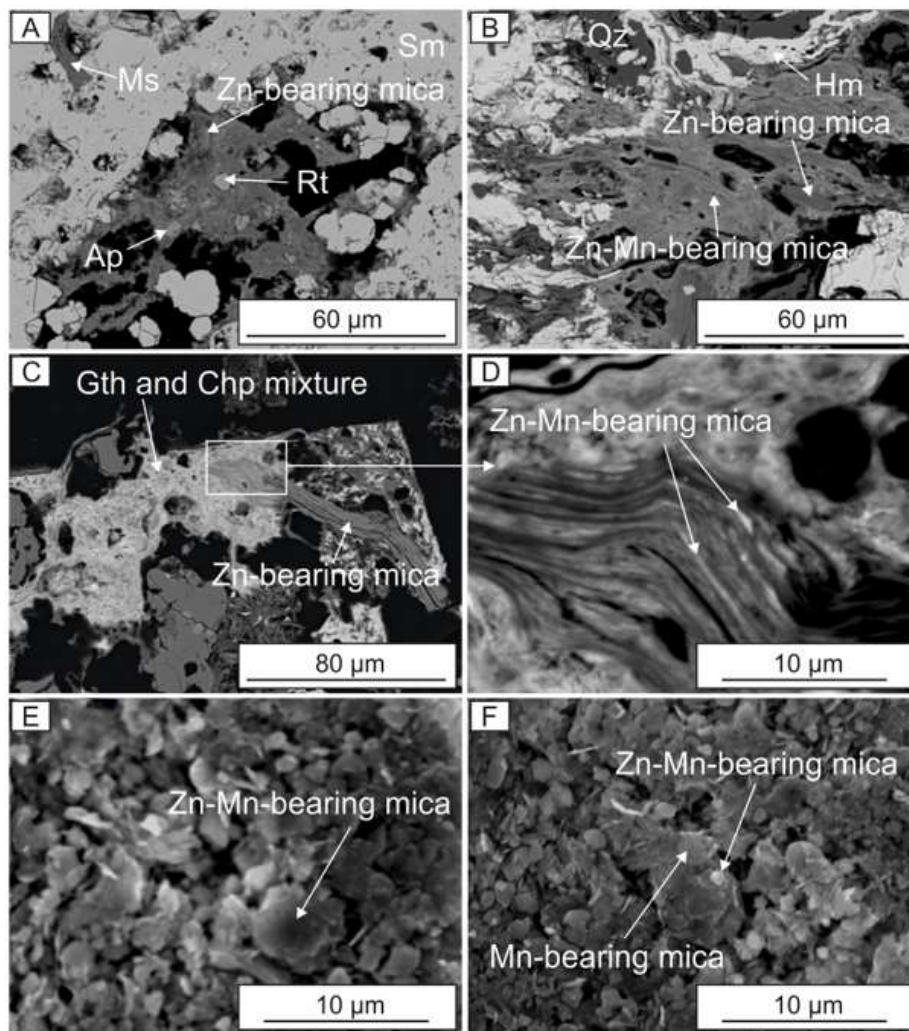


Figure 5. Secondary and backscattered electron (BSE) images of Zn-bearing and Zn-Mn-bearing micas in the Cristal samples. (A) A cavity in smithsonite (Sm) filled by a clayey mixture, which surrounds the Zn-bearing mica remnants, as well as rutile (Rt) and apatite (Ap) crystals (sample CR03-3); (B) Hendricksite surrounding a Zn-bearing mica in a hemimorphite (Hm)- and quartz (Qz)-rich sample (CR13-6); (C) Goethite (Gth) and chalcophanite (Chp) surrounding a Zn-bearing mica with possible Zn-Mn-bearing layers; (D) (sample CR13-7); (E,F) Possible Mn-(hydr)oxides-free powders from the CR07-11_5/5000 sample showing the occurrence of hendricksite flakes.

In the samples from Mina Grande fraipontite and zaccagnaite, which were already identified with XRD analyses, have been also detected by SEM-EDS (Table 2). Observed in thin section, fraipontite is always texturally associated with Zn-bearing illite or I/S, and/or with zaccagnaite (Figure 6D–F). When in association with Zn-bearing illite or I/S, fraipontite occurs as thin halos around the mica grains (Figure 6E), while if associated with zaccagnaite, it can be found as patchy remnants in the latter mineral (Figure 6D,F). Zaccagnaite also turns up as cavity filling, where it shows euhedral crystal shapes. The zaccagnaite-fraipontite association generally occurs in a clayey matrix, consisting of

Zn-bearing micas. For this reason, SEM-EDS analyses do not permit the identification of fraipontite in the Cristal mineralization with certainty.

The EDS analyses of the Bongará samples evidenced also that the smectite recognized in the XRD patterns has a sauconite composition (Table 2). The best examples could be seen in samples CR07-13 and CR03-3 (Figure 6A–C, respectively). In the latter, sauconite replacing the detrital muscovite can also be seen.

In the SEM images, the smectite group minerals show flared, “cornflake”, or “oak leaf” textures that are commonly covered by thin crusts of micrometric goethite concretions (Figure 6A). The smectites are tightly associated with other flat-lying flakes with scalloped and slightly curled edges. Such textures are generally associated with a mineral with a hybrid illite-smectite morphology [60], which from EDS analysis also results Zn-bearing (Figure 6B).

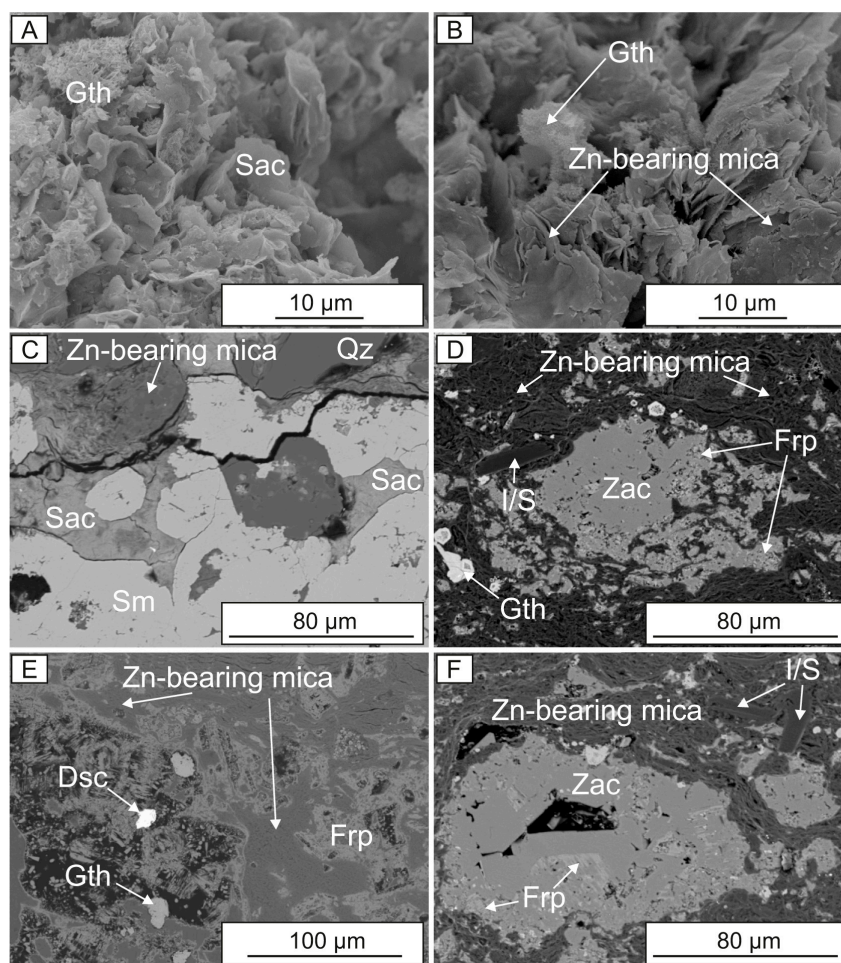


Figure 6. Secondary and backscattered electron (BSE) images of clay minerals from Cristal (A–C) and Mina Grande (D–F) deposits; (A,B) 3D images of sauconite (Sac) and interstratified I/S showing “cornflake” (sauconite) and “flat-lying flake” (Zn-bearing illite or I/S) textures. The latter are commonly obliterated by thin crusts of micrometric goethite (Gth) concretions; (C) Sauconite surrounding Zn-bearing mica and filling fractures in smithsonite (Sm) (sample CR03-3); (D–F) Zaccagnaite (Zac) replacing fraipontite (Frp), and occurring in cavities of Zn-bearing I/S. Goethite (Gth) and descloizite (Dsc) are commonly found in this mineral assemblage (sample ZB-1).

Table 1. Chemical composition and structural formulae (apfu) of Zn-bearing micas from the Cristal (CR samples) and Mina Grande (ZB samples) deposits.

Location	Cristal										Mina Grande		
Sample ID	CR03-3	CR03-3	CR03-3	CR03-3	CR07-13	CR07-13	CR13-5	CR13-6	CR13-6	CR13-6	CR13-7	ZB1	ZB1
wt %													
SiO ₂	48.17	56.84	50.97	53.00	48.60	47.41	47.42	49.94	51.33	43.19	47.25	46.10	47.17
TiO ₂	0.24	0.42	0.13	0.26	0.45	0.45	0.14	0.26	0.33	0.11	0.37	0.17	0.16
Al ₂ O ₃	28.33	22.37	20.34	25.70	29.13	36.35	26.69	29.34	25.54	26.72	25.02	36.84	27.71
MgO	2.12	1.90	2.99	3.48	1.89	0.99	2.22	2.27	3.14	1.67	2.56	-	2.72
MnO	0.22	0.15	0.09	-	-	0.24	1.66	-	0.39	5.75	1.06	0.08	-
FeO _t ^a	4.25	1.83	1.60	1.66	5.06	0.82	3.49	0.79	1.34	0.68	2.48	1.27	1.07
ZnO	0.85	2.82	12.61	1.10	0.06	0.55	0.92	3.83	5.49	8.11	5.85	0.70	9.28
K ₂ O	10.90	7.01	6.04	9.13	10.92	10.16	10.67	8.52	6.60	8.02	8.50	11.64	7.63
CaO	-	0.25	0.60	0.36	0.22	-	0.44	0.80	0.38	0.39	0.17	-	0.30
PbO	-	-	0.15	-	-	-	-	0.49	-	0.40	0.20	0.06	0.24
Total	95.08	93.59	95.54	94.69	96.33	96.97	93.64	96.24	94.55	95.04	93.46	96.87	96.28
apfu													
On the Basis of 11 O													
Si	3.29	3.79	3.55	3.52	3.27	3.09	3.28	3.32	3.46	3.10	3.33	3.04	3.23
Al	0.71	0.21	0.45	0.48	0.73	0.91	0.72	0.68	0.54	0.90	0.67	0.96	0.77
Σ _T	4.00	4.00	4.00	4.00	4.00	4.00	4.00	4.00	4.00	4.00	4.00	4.00	4.00
Al	1.57	1.55	1.22	1.53	1.58	1.88	1.45	1.62	1.49	1.36	1.41	1.90	1.47
Ti	0.01	0.02	0.01	0.01	0.02	0.02	0.01	0.01	0.02	0.01	0.02	0.01	0.01
Mg	0.22	0.19	0.31	0.34	0.19	0.10	0.23	0.22	0.32	0.18	0.27	-	0.28
Mn	0.01	0.01	0.01	-	-	0.01	0.10	-	0.02	0.35	0.06	-	-
Fe	0.24	0.10	0.09	0.09	0.28	0.04	0.20	0.04	0.08	0.04	0.15	0.07	0.06
Zn	0.04	0.14	0.65	0.05	-	0.03	0.05	0.19	0.27	0.43	0.30	0.03	0.47
Pb	-	-	0.003	-	-	-	-	0.01	-	0.01	-	-	-
Σ _O	2.09	2.01	2.28	2.03	2.06	2.08	2.03	2.09	2.20	2.37	2.21	2.01	2.28
Ca	-	0.02	0.05	0.03	0.02	-	0.03	0.06	0.03	0.03	0.01	-	0.02
K	0.95	0.60	0.54	0.77	0.94	0.84	0.94	0.72	0.57	0.73	0.76	0.98	0.67
Σ _I	0.95	0.62	0.59	0.80	0.96	0.84	0.97	0.77	0.59	0.76	0.77	0.98	0.69
Σ _{ch(T)}	-0.71	-0.21	-0.45	-0.48	-0.73	-0.91	-0.72	-0.68	-0.54	-0.90	-0.67	-0.96	-0.77
Σ _{ch(O)}	-0.24	-0.43	-0.19	-0.35	-0.25	0.07	-0.28	-0.16	-0.09	0.11	-0.11	-0.02	0.06
Σ _{ch(I)}	0.95	0.64	0.64	0.83	0.98	0.84	1.00	0.84	0.63	0.79	0.78	0.98	0.71

Note: ^a FeO_t as total iron; apfu = atoms per formula unit; - not determined.

Table 2. Chemical compositions and structural formulae (apfu) of trioctahedral mineral species from the Mina Grande (fraipontite) and Cristal (sauconite and Zn-Mn-bearing mica) deposits.

Location	Mina Grande			Cristal				
Sample ID	ZB1		CR03-3	CR07-9	CR13-6	CR13-6		
Mineral	Fraipontite		Sauconite	Zn-Mn-Bearing Mica				
wt %								
SiO ₂	19.64	16.35	37.78	37.88	40.44	35.99	34.86	38.99
TiO ₂	-	-	0.12	0.12	0.13	0.12	-	0.17
Al ₂ O ₃	20.41	20.46	6.52	5.08	7.11	18.21	20.15	23.13
MgO	0.07	0.05	0.78	0.47	0.75	2.18	1.64	1.67
MnO	0.05	-	-	-	-	9.97	10.89	7.85
FeO _t ^a	0.77	0.32	0.35	0.27	0.11	2.59	1.42	0.66
ZnO	46.67	49.16	37.00	40.24	34.73	19.17	16.85	13.15
CaO	0.04	-	1.52	0.95	1.00	0.38	0.11	0.17
K ₂ O	-	0.01	0.73	0.15	1.15	4.56	5.61	6.86
PbO	-	0.21	-	-	-	-	1.18	0.57
Total	87.65	86.56	84.80	85.16	85.42	93.15	92.71	93.23
apfu	On the Basis of 14 O		On the Basis of 11 O		On the Basis of 11 O			
Si	2.48	2.15	3.52	3.57	3.64	2.92	2.85	2.99
Al	1.52	1.85	0.48	0.43	0.36	1.08	1.15	1.01
Σ _T	4.00	4.00	4.00	4.00	4.00	4.00	4.00	4.00
Al	1.52	1.32	0.24	0.13	0.39	0.66	0.79	1.08
Ti	-	-	0.01	0.01	0.01	0.01	-	0.01
Mg	0.01	0.04	0.11	0.07	0.10	0.26	0.20	0.19
Mn	0.01	0.01	-	-	-	0.68	0.75	0.51
Fe	0.08	0.11	0.03	0.02	0.01	0.18	0.10	0.04
Zn	4.36	4.76	2.54	2.80	2.31	1.15	1.02	0.75
Pb	-	0.02	-	-	-	-	0.03	0.01
Σ _O	5.98	6.26	2.93	3.03	2.82	2.94	2.89	2.59
Ca	0.01	-	0.15	0.10	0.10	0.03	0.01	0.01
K	-	0.03	0.09	0.02	0.13	0.47	0.58	0.67
Σ _I	0.01	0.03	0.24	0.12	0.23	0.50	0.59	0.68
Σ _{ch(T)}	-1.52	-1.85	-0.48	-0.43	-0.36	-1.08	-1.15	-1.01
Σ _{ch(O)}	1.50	1.82	0.09	0.21	0.03	0.55	0.55	0.32
Σ _{ch(I)}	0.02	0.03	0.39	0.22	0.33	0.53	0.60	0.69

5. Discussion

The XRPD analyses and the microscopic observations carried out on the samples from the Cristal and Mina Grande deposits have revealed the presence of layered silicates belonging to mica, smectite, and kaolinite-serpentine groups. In both deposits, mica is mostly represented by illite or I/S mixed layers. The EDS analyses on the I/S mixed layers have shown that in these phases, the Zn and K concentrations are inversely correlated (Table 1). This could suggest that in the I/S, Zn is partly hosted by smectite layers, which are characterized by sauconite composition, and that Zn consequently increases as the illite component decreases. Textural observations would suggest that the original illite or I/S mixed layers were of detrital or sedimentary origin (e.g., I/S mixed layers show *Reichweite values* “R” > 1, which are commonly produced by diagenetic processes [55]. Looking at the existing literature [29,31], Zn incorporation in these phyllosilicates could be related either to the same hydrothermal processes that are responsible for the emplacement of sulfides [34,35], or to supergene alteration, which allowed for the formation of nonsulfide ores. In both cases, Zn incorporation into the I/S also produced an increase of the smectite (i.e., sauconite) component in the mixed layer. However, we cannot exclude that part of the detected sauconite that overgrows the I/S grains, instead of being incorporated into the mixed layers, using the I/S lamellae as a template on which smectite crystallizes directly from fluids, as already observed in other deposits [29,31].

In several mica-rich samples, Zn-Mn-bearing phyllosilicates with a chemical composition similar to that of hendricksite were also detected as fine intergrowths between the other phyllosilicates, i.e., Zn-bearing I/S and saucosite. In the $M^+-4Si-3R^{2+}$ ternary plot (Figure 7), which is useful to distinguish between dioctahedral and trioctahedral clay types [61], the compositions of the micas describe the cluster of points “A-B-C”, and are mostly dispersed along the axis “A-B”, which spans between the muscovite and saucosite end-members. In this diagram, it is also possible to see that the compositions of Zn-bearing micas (illite or I/S) are closer to the muscovite than to the saucosite end-member, whereas the Zn-Mn-bearing micas are closer to the saucosite than to the hendricksite end-member. This distribution is compatible with the nature of the Zn-bearing micas reported before, which probably consist of illite or I/S, with a high % illite, and saucosite as the smectitic component. A possible explanation of the fact that the compositions of Zn-Mn-bearing micas do not converge exactly toward the hendricksite composition, can be found in the texture of these phyllosilicates, which being finely intergrown with saucosite and Zn-bearing I/S mixed layers, cannot be analyzed by SEM-EDS with extreme precision. In other words, saucosite, grown over the hendricksite, or directly formed at its expenses, can generate considerable bias in the EDS analysis of hendricksite. However, it is important to consider that hendricksite is a mineral that is typical of Zn-oxidized hypogene mineralizations [1]. In fact, hendricksite has been recognized for the first time in stratiform hypogene deposits e.g., Franklin mine, Franklin, NJ, USA; [62], and in many Zn-bearing skarns [63], where it is derived from high temperature hydrothermal processes ($T > 200\text{ }^\circ\text{C}$). These high temperatures have been corroborated by the unsuccessful attempts to synthesize Zn- and Mn-bearing micas at temperatures lower than $55\text{ }^\circ\text{C}$ [32,64], which would be typical of a supergene environment ($25\text{ }^\circ\text{C}$ and 1 atm). Therefore, it is likely that also in the Cristal prospect hendricksite formed from hydrothermal fluids, which have emplaced also the sulfide mineralization.

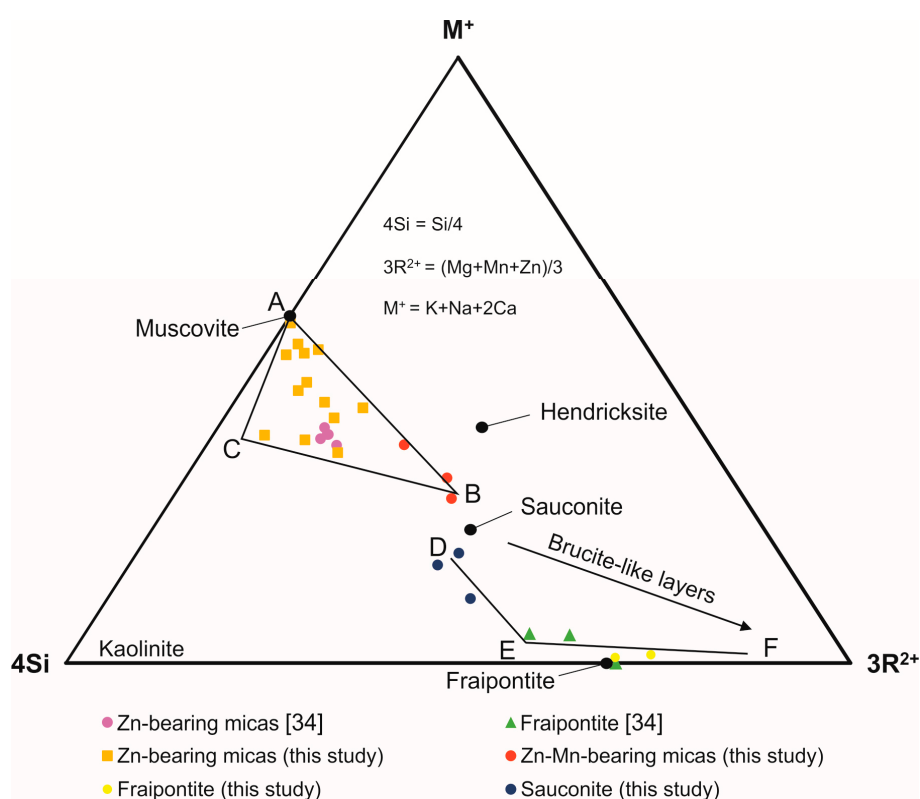


Figure 7. $4Si-M^+-3R^{2+}$ ternary diagram showing the chemical compositions of micas and clays identified in the Cristal and Mina Grande samples. Muscovite, hendricksite, saucosite, and fraipontite compositions, as reported in the IMA database. Due to the compositions of the studied minerals, for the calculation of the $3R^{2+}$ component Mn was used instead of Fe.

The peculiar fraipontite-zaccagnaite association that was observed at Mina Grande might also be genetically related either to hydrothermal or to supergene processes. In fact, this association was observed in marble quarries of the Carrara basin (Apuane Alps, Italy), where it was deposited through the hydrothermal alteration of Zn-bearing sulfides and sulfosalts, in the presence of aluminum-rich fluids [58]. However, zaccagnaite and fraipontite can also form from supergene fluids, as a product of sulfide weathering [27,59]. The XRD analysis of zaccagnaite from the Mina Grande deposit points to the presence of the zaccagnaite 3R-polytype, which was firstly identified in the El Soplao karstic caves (Cantabria, Spain), where it was considered as having been formed at ~11 °C in a supergene environment [59]. The latter formation temperature is very similar to that (~15 °C) calculated for some supergene minerals in the Mina Grande deposit [34], and would therefore be perfectly compatible with the formation of zaccagnaite in a supergene environment at Mina Grande. In the same deposit, however, it was still not possible to definitely establish the nature of fraipontite. In fact, this mineral may have been formed either during the hydrothermal process that generated the sulfides, or in the early stages of supergene alteration, which took place under acidic conditions that are associated with the alteration of sulfides. In both cases, when the buffering of the carbonate host rock turned the environment from acidic to alkaline (pH > 7), fraipontite became unstable and zaccagnaite started to form at its expense.

6. Conclusions

This study has implemented the data on Zn-bearing phyllosilicates from the Cristal and Mina Grande (Bongará) mineralized areas, also providing a new insight on their genesis. In both deposits, several types of phyllosilicates have been detected, which consist of micas and clay minerals. The micas mainly correspond to I/S mixed layers of detrital origin, which have been partly altered or overprinted by saucornite of either supergene or hydrothermal origin. Hendricksite occurring sporadically in the Cristal prospect may be considered as a hydrothermal product, which is formed during the emplacement of sulfides. In the Mina Grande deposit, a peculiar association of fraipontite and zaccagnaite was observed. Even though both of these minerals can be either of hydrothermal or supergene origin, the identified zaccagnaite polytype suggests that fraipontite and zaccagnaite are both genetically derived from weathering processes. Ongoing mineralogical investigations carried out by high-resolution transmission electron microscopy (HRTEM) will hopefully better constrain the nature of the Zn-bearing clay minerals in the Bongará district.

Acknowledgments: This work is part of G.A.'s ongoing Ph.D. thesis at the Università di Napoli Federico II (Italy). G.A. and co-authors are indebted to the Compañía Minera Pilar del Amazonas, and to Zinc One Resources Inc. for allowing publication. Part of this study was funded by a Student Research Grant (Project SRG_15-40) from the Society of Economic Geologists Canada Foundation (SEGCF) to G.A. and by the European Union's Horizon 2020 research and innovation program, supporting a Marie Skłodowska-Curie Individual Fellowship (Project Number 660885) to N.M.

Author Contributions: Giuseppe Arfè, Nicola Mondillo, Maria Boni and Tommaso Di Palma participated to the sampling campaign in Peru. Giuseppe Arfè and Tommaso Di Palma carried out sample preparation and laboratory work. Giuseppina Balassone and Piergiulio Cappelletti performed the XRD analysis. The article was primarily written by Giuseppe Arfè, Nicola Mondillo and Maria Boni, and then revised by the other co-authors.

Conflicts of Interest: The authors declare no conflict of interest.

References

1. Hitzman, M.W.; Reynolds, N.A.; Sangster, D.F.; Allen, C.R.; Carman, C.E. Classification, genesis, and exploration guides for nonsulfide Zinc deposits. *Econ. Geol.* **2003**, *98*, 685–714. [[CrossRef](#)]
2. Boni, M.; Mondillo, N. The “Calamines” and the “Others”: The great family of supergene nonsulfide zinc ores. *Ore Geol. Rev.* **2015**, *67*, 208–233. [[CrossRef](#)]
3. Borg, G. A review of supergene nonsulphide zinc (SNSZ) deposits—The 2014 update. In *Current Perspectives of Zinc Deposits*; Archibald, S.M., Piercey, S.J., Eds.; Irish Association for Economic Geology: Dublin, Ireland; pp. 123–147, ISBN 978-0-9509894-5-7.

4. Borg, G.; Kärner, K.; Buxton, M.; Armstrong, R.; Merwe, S.W. Geology of the Skorpion supergene Zn deposit, southern Namibia. *Econ. Geol.* **2003**, *98*, 749–771. [[CrossRef](#)]
5. Kärner, K. The Metallogeneses of the Skorpion Non-Sulphide Zinc Deposit, Namibia. Ph.D. Thesis, Martin-Luther-Universität Halle-Wittenberg, Halle, Germany, July 2006.
6. Connelly, D. High clay ores: A mineral processing nightmare part 2. *Aust. J. Min.* **2011**, *24*, 28–29.
7. Lim, J. Controlling Clay Behaviour in Suspension: Developing a New Paradigm for the Minerals Industry. Ph.D. Thesis, University of Melbourne, Melbourne, Australia, April 2011.
8. Boni, M.; Schmidt, P.R.; de Wet, J.R.; Singleton, J.D.; Balassone, G.; Mondillo, N. Mineralogical signature of nonsulfide zinc ores at Accha (Peru): A key for recovery. *Int. J. Miner. Process.* **2009**, *93*, 267–277. [[CrossRef](#)]
9. Rollinson, G.; Andersen, J.C.Ø.; Stickland, R.J.; Boni, M.; Fairhurst, R. Characterization of non-sulphide zinc deposits using QEMSCAN. *Miner. Eng.* **2011**, *24*, 778–787. [[CrossRef](#)]
10. Kademli, M.; Gulzoy, O.Y. The role of particle size and solid contents of feed on mica-feldspar separation in gravity concentration. *Physicochem. Probl. Miner. Process.* **2012**, *48*, 645–654. [[CrossRef](#)]
11. Bayraktar, I.; Aslan, A.; Ersayin, S. Effects of primary slime and clay on selectivity of flotation of sub-volcanogenic complex polymetallic ores. *Trans. Inst. Min. Metall. Sect. B* **1998**, *107*, C71–C76.
12. Fuerstenau, M.C.; Chander, S.; Woods, R. Sulfide mineral flotation. In *Froth Flotation: A Century of Innovation*; Fuerstenau, M.C., Jameson, G., Yoon, R.-H., Eds.; SME: Littleton, CO, USA; pp. 425–464, ISBN-13 978-0873352529; ISBN-10 0873352521.
13. Gnoinski, J. Skorpion Zinc: Optimization and innovation. *J. S. Afr. Inst. Min. Metall.* **2007**, *107*, 657–662.
14. De Wet, J.R.; Singleton, J.D. Development of a viable process for the recovery of zinc from oxide ores. *J. S. Afr. Inst. Min. Metall.* **2008**, *108*, 253–259.
15. Abkhoshk, E.; Jorjani, E.; Al-Harashsheh, M.S.; Rashchi, F.; Naazeri, M. Review of the hydrometallurgical processing of non-sulfide zinc ores. *Hydrometallurgy* **2014**, *149*, 153–167. [[CrossRef](#)]
16. Tiller, K.G.; Pickering, J.G. The synthesis of zinc silicates at 20 °C and atmospheric pressure. *Clays Clay Miner.* **1974**, *22*, 409–416. [[CrossRef](#)]
17. Harder, H. Clay mineral formation under lateritic weathering conditions. *Clay Miner.* **1977**, *12*, 281–288. [[CrossRef](#)]
18. Kittrick, J.A. Soil minerals in the Al₂O₃-SiO₂-H₂O system and a theory of their formation. *Clays Clay Miner.* **1969**, *17*, 157–167. [[CrossRef](#)]
19. Sherman, D.M. *Weathering Reactions and Soil-Groundwater Chemistry*; Lecture Notes 2001/2002; Environmental Geochemistry, University of Bristol: Bristol, UK, 2001.
20. Roy, D.M.; Mumpton, F.A. Stability of minerals in the system ZnO-SiO₂-H₂O. *Econ. Geol.* **1956**, *51*, 432–443. [[CrossRef](#)]
21. Klopogge, T.; Komarneni, S.; Amonette, J. Synthesis of smectite clay minerals: A critical review. *Clays Clay Miner.* **1999**, *47*, 529–554. [[CrossRef](#)]
22. Higashi, S.; Miki, K.; Komarneni, S. Hydrothermal synthesis of Zn-smectite. *Clays Clay Miner.* **2002**, *50*, 299–305. [[CrossRef](#)]
23. Petit, S.; Rigbi, D.; Decarreau, A. Transformation of synthetic Zn-stevensite to Zn-talc induced by the Hofmann-Klemen effect. *Clays Clay Miner.* **2008**, *56*, 645–654. [[CrossRef](#)]
24. Pascua, C.S.; Ohnuma, M.; Matsushita, Y.; Tamura, K.; Yamada, H.; Cuadros, J.; Ye, J. Synthesis of monodisperse Zn-smectite. *Appl. Clay Sci.* **2010**, *48*, 55–59. [[CrossRef](#)]
25. Garrels, R.M.; Christ, C.L. *Solutions, Minerals, and Equilibria*, 1st ed.; Harpers' Geoscience Series; Harper and Row: New York, NY, USA; 450p, ISBN 13 9780877353331.
26. Coppola, V.; Boni, M.; Gilg, H.A.; Balassone, G.; Dejonghe, L. The “calamine” nonsulfide Zn-Pb deposits of Belgium: Petrographical, mineralogical and geochemical characterization. *Ore Geol. Rev.* **2008**, *33*, 187–210. [[CrossRef](#)]
27. Choulet, F.; Buatier, M.; Barbanson, L.; Guégan, R.; Ennaciri, A. Zinc-rich clays in supergene non-sulfide zinc deposits. *Miner. Depos.* **2016**, *51*, 467–490. [[CrossRef](#)]
28. Will, P.; Friedrich, F.; Hochleitner, R.; Gilg, H.A. Fraipontite in the hydrothermally overprinted oxidation zone of the Preguiça mine, Southern Portugal. In Proceedings of the Mid-European Clay Conference, Dresden, Germany, 16–19 September 2014.
29. Mondillo, N.; Nieto, F.; Balassone, G. Micro- and nano-characterization of Zn-clays in nonsulfide supergene ores of southern Peru. *Am. Mineral.* **2015**, *100*, 2484–2496. [[CrossRef](#)]

30. Buatier, M.; Choulet, F.; Petit, S.; Chassagnon, R.; Vennemann, T. Nature and origin of natural Zn clay minerals from the Bou Arhous Zn ore deposit: Evidence from electron microscopy (SEM-TEM) and stable isotope compositions (H and O). *Appl. Clay Sci.* **2016**, *132*, 377–390. [[CrossRef](#)]
31. Balassone, G.; Nieto, F.; Arfè, G.; Boni, M.; Mondillo, N. Zn-clay minerals in the nonsulfide orebody of Skorpion (Namibia): Identification and genetic clues revealed by HRTEM and AEM study. *Appl. Clay Sci.* **2017**, *150*, 309–322. [[CrossRef](#)]
32. Choi, J.; Komarneni, S.; Grover, K.; Katsuki, H.; Park, M. Hydrothermal synthesis of Mn-mica. *Appl. Clay Sci.* **2009**, *46*, 69–72. [[CrossRef](#)]
33. Sharygin, V. Zincian micas from peralkaline phonolites of the Oktyabrsky massif, Azov Sea region, Ukrainian Shield. *Eur. J. Min.* **2015**, *27*, 521–533. [[CrossRef](#)]
34. Arfè, G.; Mondillo, N.; Boni, M.; Balassone, G.; Joachimski, M.; Mormone, A.; Di Palma, T. The karst hosted Mina Grande nonsulfide zinc deposit, Bongará district (Amazonas region, Peru). *Econ. Geol.* **2017**, *112*, 1089–1110. [[CrossRef](#)]
35. Arfè, G.; Mondillo, N.; Boni, M.; Joachimski, M.; Balassone, G.; Mormone, A.; Santoro, L.; Castro Medrano, E. The Cristal Zn prospect (Amazonas region, Northern Peru). Part II: An example of supergene zinc enrichments in tropical areas. *Ore Geol. Rev.* **2017**. under review.
36. Rosas, S.; Fontboté, L.; Tankard, A. Tectonic evolution and paleogeography of the Mesozoic Pucará basin, central Peru. *J. S. Am. Earth Sci.* **2007**, *24*, 1–24. [[CrossRef](#)]
37. Spikings, R.; Reitsma, M.J.; Boekhout, F.; Mišković, A.; Ulianov, A.; Chiaradia, M.; Gerdes, A.; Schaltegger, U. Characterisation of Triassic rifting in Peru and implications for the early disassembly of western Pangaea. *Gondwana Res.* **2016**, *35*, 124–143. [[CrossRef](#)]
38. Reid, C.J. Stratigraphy and Mineralization of the Bongara MVT Zinc-Lead District, Northern Peru. Master's Thesis, University of Toronto, Toronto, ON, Canada, 2001.
39. Mišković, A.; Spikings, R.A.; Chew, D.M.; Košler, J.; Ulianov, A.; Schaltegger, U. Tectonomagmatic evolution of Western Amazonia: Geochemical characterization and zircon U-Pb geochronologic constraints from the Peruvian Eastern Cordilleran granitoids. *Geol. Soc. Am. Bull.* **2009**, *121*, 1298–1324. [[CrossRef](#)]
40. Mégard, F. *Geología del Cuadrángulo de Huancaayo*; Servicio de Geología y Minería: Lima, Peru, 1968; 123p.
41. Szekely, T.S.; Grose, L.T. Stratigraphy of the carbonate, black shale, and phosphate of the Pucará Group (Upper Triassic-Lower Jurassic), central Andes, Peru. *Geol. Soc. Am. Bull.* **1972**, *83*, 407–428. [[CrossRef](#)]
42. Rosas, S.; Fontboté, L. Evolución sedimentológica del Grupo Pucará (Triásico superior-Jurásico inferior) en un perfil SW-NE en el centro del Perú. In *Volume Jubilar Alberto Benavides*; Sociedad Geológica del Perú: Lima, Peru, 1995; pp. 279–309.
43. Mathalone, J.M.P.; Montoya, R.M. Petroleum geology of the sub-Andean basins of Peru. *Am. Assoc. Petr. Geol. Mem.* **1995**, *62*, 423–444.
44. Instituto Geológico Minero y Metalúrgico (INGEMMET). *Geología de Los Cuadrangulos de Bagua Grande, Jumbilla, Lonya Grande, Chachapoyas, Rioja, Leimebamba y Bolivar*; Carta Geologica Nacional, Peru; Boletín 56 Serie A; Instituto Geológico Minero y Metalúrgico: Lima, Peru, 1995; 390p.
45. Gregory-Wodzicki, K.M. Uplift history of the Central Northern Andes: A review. *Geol. Soc. Am. Bull.* **2000**, *112*, 1092–1105. [[CrossRef](#)]
46. Klein, G.D.; Zúñiga y Rivero, F.G.; Hay-Roe, H.; Alvarez-Calderon, E. A Reappraisal of the Mesozoic/Cenozoic Tectonics and Sedimentary Basins of Peru. In *Search and Discover Article (AAPG)*; AAPG/Datapages, Inc.: Tulsa, OK, USA, 2011; 55p.
47. Pfiffner, O.A.; Gonzalez, L. Mesozoic-Cenozoic evolution of the Western Margin of South America: Case study of the Peruvian Andes. *Geosciences* **2013**, *3*, 262–310. [[CrossRef](#)]
48. Brophy, J.A. *Rio Cristal Resources Corp., Bongará Zinc Project*; NI 43-101 Technical Report; SMV-Superintendencia del Mercado de Valores: Lima, Peru, 2012; 104p.
49. Mondillo, N.; Arfè, G.; Boni, M.; Balassone, G.; Boyce, A.; Joachimski, M.; Villa, I.M. The Cristal Zinc Zn prospect (Amazonas region, Northern Peru). Part I: New insights on the sulfide mineralization in the Bongará province. *Ore Geol. Rev.* **2017**, under review.
50. Basuki, N.I.; Spooner, E.T.C. Fluid evolution and flow direction of MVT Zn-Pb related basinal brines, Bongará area, northern Peru: CL and fluid inclusion data. In Proceedings of the Geological-Mineralogical Association of Canada-Society of Economic Geologists—Society for Geology Applied to Mineral Deposits Meeting, Quebec City, QC, Canada, 26–28 May 2008.

51. Basuki, N.I.; Spooner, E.T.C. Post-early Cretaceous Mississippi Valley Type Zn-Pb mineralization in the Bongará Area, Northern Peru: Fluid evolution and Paleo-Flow from fluid inclusions evidence. *Explor. Min. Geol.* **2009**, *18*, 25–39. [[CrossRef](#)]
52. Basuki, N.I.; Taylor, B.E.; Spooner, E.T.C. Sulfur Isotope Evidence for Thermochemical Reduction of Dissolved Sulfate in Mississippi Valley-Type Zinc-Lead Mineralization, Bongara Area, Northern Peru. *Econ. Geol.* **2008**, *103*, 783–799. [[CrossRef](#)]
53. Mondillo, N.; Arfè, G.; Herrington, R.; Boni, M.; Wilkinson, C.; Mormone, A. Possible economic enrichments of Ge in supergene settings: Evidence from the Cristal supergene Zn nonsulfide prospect, Bongará district, Northern Peru. *Miner. Depos.* **2017**. under review.
54. Workman, A.; Breede, K. *Technical Report on the Bongará Zinc Project in the Yambrasbamba Area, Northern Peru*; NI 43-101 Technical Report; Watts, Griffis and McQuat Limited Consulting Geologists and Engineers: Toronto, ON, Canada, 2016; 139p.
55. Moore, D.M.; Reynolds, R.C. *X-ray Diffraction and the Identification and Analysis of Clay Minerals*; Oxford University Press: New York, NY, USA, 1997; 378p, ISBN 9780195087130.
56. Brunton, G. Vapour pressure glycolation of oriented clay minerals. *Am. Mineral.* **1955**, *40*, 124–126.
57. Drits, V.A.; Sokolova, T.N.; Sokolova, G.V.; Cherkashin, V.I. New members of the hydrotalcite-manasseite group. *Clays Clay Miner.* **1987**, *35*, 401–417. [[CrossRef](#)]
58. Merlino, S.; Orlandi, P. Carraraite and zaccagnaite, two new minerals from the Carrara marble quarries: Their chemical compositions, physical properties, and structural features. *Am. Mineral.* **2001**, *86*, 1293–1301. [[CrossRef](#)]
59. Lozano, R.P.; Rossi, C.; La Iglesia, Á.; Matesanz, E. Zaccagnaite-3R, a new Zn-Al hydrotalcite polytype from El Soplao cave (Cantabria, Spain). *Am. Mineral.* **2012**, *97*, 513–523. [[CrossRef](#)]
60. Keller, W.D.; Reynolds, R.C.; Inque, A. Morphology of clay minerals in the smectite-to-illite conversion series by scanning electron microscopy. *Clays Clay Miner.* **1986**, *34*, 187–197. [[CrossRef](#)]
61. Meunier, A. *Clays*; Springer: Berlin/Heidelberg, Germany, 2005; 476p, ISBN 3-540-21667-7.
62. Frondel, C.; Ito, J. Hendricksite: A new species of mica. *Am. Mineral.* **1966**, *51*, 1107–1127.
63. Leavens, P.B.; Zullo, J.; Verbeek, E. A complex, genthelvite-bearing skarn from the Passaic pit, Sterling Hill mine, Ogdensburg, New Jersey. *Axis* **2009**, *5*, 1–26.
64. Perrotta, A.J.; Garland, T.J. Low Temperature Synthesis of Zinc-Phlogopite. *Am. Mineral.* **1975**, *60*, 152–154.



© 2017 by the authors. Licensee MDPI, Basel, Switzerland. This article is an open access article distributed under the terms and conditions of the Creative Commons Attribution (CC BY) license (<http://creativecommons.org/licenses/by/4.0/>).